

Deep Synoptic Array science: a 50 Mpc fast radio burst constrains the mass of the Milky Way circumgalactic medium

VIKRAM RAVI,^{1,2} MORGAN CATHA,² GE CHEN,¹ LIAM CONNOR,¹ JAMES M. CORDES,^{3,4} JAKOB T. FABER,¹
JAMES W. LAMB,² GREGG HALLINAN,^{1,2} CHARLIE HARNACH,² GREG HELLBOURG,^{1,2} RICK HOBBS,² DAVID HODGE,¹
MARK HODGES,² CASEY LAW,^{1,2} PAUL RASMUSSEN,² KRITTI SHARMA,¹ MYLES B. SHERMAN,¹ JUN SHI,¹ DANA SIMARD,¹
JEAN J. SOMALWAR,¹ REYNIER SQUILLACE,¹ SANDER WEINREB,¹ DAVID P. WOODY,² NITIKA YADLAPALLI,¹

(THE DEEP SYNOPTIC ARRAY TEAM)

¹*Cahill Center for Astronomy and Astrophysics, MC 249-17 California Institute of Technology, Pasadena CA 91125, USA.*

²*Owens Valley Radio Observatory, California Institute of Technology, Big Pine CA 93513, USA.*

³*Department of Astronomy, Cornell University, Ithaca, NY 14853, USA*

⁴*Cornell Center for Astrophysics and Planetary Science and Department of Astronomy, Cornell University, Ithaca, NY 14853, USA*

ABSTRACT

We present the Deep Synoptic Array (DSA-110) discovery and interferometric localization of the so far non-repeating FRB 20220319D. The FRB originates in a young, rapidly star-forming barred spiral galaxy, IRAS 02044+7048, at just 50 Mpc. Although the NE2001 and YMW16 models for the Galactic interstellar-medium (ISM) contribution to the DM of FRB 20220319D exceed its total observed DM, we show that uncertainties in these models accommodate an extragalactic origin for the burst. We derive a conservative upper limit on the DM contributed by the circumgalactic medium (CGM) of the Milky Way: the limit is either 28.7 pc cm^{-3} and 47.3 pc cm^{-3} , depending on which of two pulsars nearby on the sky to FRB 20220319D is used to estimate the ISM DM. These limits both imply that the total Galactic CGM mass is $< 10^{11} M_{\odot}$, and that the baryonic mass of the Milky Way is $\lesssim 60\%$ of the cosmological average given the total halo mass. More stringent albeit less conservative constraints are possible when the DMs of pulsars in the distant globular cluster M53 are additionally considered. Although our constraints are sensitive to possible anisotropy in the CGM and to the assumed form of the radial-density profile, they are not subject to uncertainties in the chemical and thermal properties of the CGM. Our results strongly support scenarios commonly predicted by galaxy-formation simulations wherein feedback processes expel baryonic matter from the halos of galaxies like the Milky Way.

Keywords: Barred spiral galaxies — circumgalactic medium — radio interferometers — radio transient sources — star formation — warm ionized medium

1. INTRODUCTION

Galaxies like the Milky Way are embedded in a multi-phase ($\sim 10^4 - 10^7 \text{ K}$), highly ionized (hydrogen neutral fractions $\ll 0.01\%$), kinematically complex, spatially clumpy and anisotropic circumgalactic medium (CGM; Tumlinson et al. 2017). Likely extending beyond dark-matter halo virial radii r_{vir} , the CGM may represent the dominant baryon component by mass within

halos. The physical properties of the CGM of external galaxies, including density, temperature, kinematic structure, and chemical composition have long been probed by absorption-line measurements towards background objects. More recently, detections of thermal bremsstrahlung (e.g., Li et al. 2018) and the Sunyaev-Zeldovich effect around nearby galaxies (e.g., Bregman et al. 2022) provide independent constraints on the CGM density and temperature structure, potentially confirming the presence of extended coronae around galaxies. Evidence for extended gas reservoirs associated with nearby galaxies, either in the CGM or the intra-group medium, has also been observed in the dis-

persion measures (DMs) of background fast radio bursts (FRBs; Connor & Ravi 2022; Wu & McQuinn 2022). Galaxy-formation simulations highlight the dependence of CGM properties on feedback from stellar winds, supernovae, and AGN, as well as on the galaxy merger histories (e.g., Wijers et al. 2020; Hafen et al. 2020; Zheng et al. 2020; Fielding et al. 2020; Appleby et al. 2021; Ramesh et al. 2022). The simulations predict varying degrees of anisotropy in the CGM of individual galaxies, and different total CGM masses for galaxies with comparable global characteristics. A ubiquitous prediction of simulations is that feedback processes determine the integrated CGM mass, M_{CGM} . In general, CGM baryon fractions $f_{\text{CGM}} = \frac{M_{\text{CGM}}\Omega_M}{M_{\text{tot}}\Omega_b} \lesssim 0.5$ are predicted, where M_{tot} is the total (dark matter and baryonic) halo mass.

A halo of $\sim 10^6$ K gas at densities $\lesssim 10^{-3} \text{ cm}^{-3}$ surrounding the Milky Way was proposed by Spitzer (1956) as a solution to the problem of confining distant cold-gas clouds at high Galactic latitudes. Tentative evidence for such coronal gas had previously been found in observations of the diffuse radio-synchrotron background (e.g., Baldwin 1956). A theoretical basis for the origins of such a hot CGM around galaxies was developed in the 1970s (Rees & Ostriker 1977; White & Rees 1978), with the gas infalling onto dark-matter halos heated to virial temperatures of $\gtrsim 10^6$ K, possibly in shocks at the halo virial radii (see also Birnboim & Dekel 2003). It would, however, be nearly two decades before further observational evidence for a hot Milky Way CGM was identified using observations of shadows in the soft X-ray background from high-latitude (Snowden et al. 1991) and high-velocity (Herbstmeier et al. 1995) cold clouds, and in the spectral decomposition of the background into absorbed and unabsorbed components (Garmire et al. 1992). Today the hot CGM of the Milky Way is best traced through X-ray observations of OVII and OVIII diffuse emission, and absorption towards bright background sources. Although high Galactic latitude data are well fit by a spheroidal component with a mass of a few $\times 10^{10} M_{\odot}$ (e.g., Bregman & Lloyd-Davies 2007; Gupta et al. 2012), more recent models include a substantially less massive ($\sim 0.1\%$), but denser disk-like component to explain the line observations (Li & Bregman 2017; Nakashima et al. 2018; Kaaret et al. 2020; Ueda et al. 2022). Structure in the hot Milky Way CGM is also observed in the form of the Fermi (Su et al. 2010), Parkes (Carretti et al. 2013) and eROSITA (Predehl et al. 2020) bubbles. The neutral and warm ($\lesssim 10^5$ K) components of the Milky Way CGM, as primarily traced through observations of high-velocity clouds, are likely sub-dominant in mass to the

hot component (few $\times 10^8 M_{\odot}$; Putman et al. 2012), but highlight the complexities of the disk-halo interface (e.g., Koo et al. 1992; Werk et al. 2019; Clark et al. 2022).

The mass of the Galactic CGM is uncertain. Here we assume $M_{\text{tot}} = 1.5 \times 10^{12} M_{\odot}$ (following Prochaska & Zheng 2019) and a total Galactic mass in stars and cold gas of $6 \times 10^{10} M_{\odot}$ (Draine 2011). Setting $f_{\text{CGM}} = 1$ and $\Omega_b/\Omega_M = 0.188$ (Planck Collaboration et al. 2020) implies $M_{\text{CGM}} = 2.82 \times 10^{11} M_{\odot}$. Recent models for the distribution of OVII and OVIII emission and absorption result in M_{CGM} values between $3 - 4 \times 10^{10} M_{\odot}$ (Li & Bregman 2017), $5.5 - 8.6 \times 10^{10} M_{\odot}$ (Kaaret et al. 2020), and $\sim 1.2 \times 10^{11} M_{\odot}$ (Yamasaki & Totani 2020). Faerman et al. (2017) argue that a portion of the hot CGM is also traced by OVI absorption, as is observed in external galaxies (Tumlinson et al. 2011), and find $M_{\text{CGM}} = 1.2 \times 10^{11} M_{\odot}$. Systematic effects that make the estimation of M_{CGM} difficult include the model uncertainties in foregrounds and in the spatial distribution and clumpiness of the gas, and the poorly constrained gas metallicity. An alternate measurement of M_{CGM} was found by Salem et al. (2015) by modeling the ram-pressure stripping of the Large Magellanic Cloud (LMC); a low value of $(2.7 \pm 1.4) \times 10^{10} M_{\odot}$ was found.

The DMs of FRBs and pulsars within the Milky Way halo offer a unique probe of the content of the Galactic CGM (e.g., Anderson & Bregman 2010; Platts et al. 2020). FRBs are transient radio emissions from distant extragalactic sources that, like the emissions from radio pulsars, are so short in duration that the dispersion in intervening plasma is evident as an arrival-time delay at lower frequencies:

$$\Delta t(\nu) = \frac{q_e^2}{2\pi m_e c \nu^2} \int_0^D n_e(l) dl, \quad (1)$$

where q_e is the electron charge, m_e is the electron mass, ν is the frequency, D is the source distance, and $n_e(l)$ is the electron number density along the sightline. Under physical conditions of CGM gas, DMs quantify the column densities along the source sightlines. In all cases, however, the observed DMs of FRBs, DM_{obs} , are composed of a selection of additive components:

$$\text{DM}_{\text{obs}} = \text{DM}_{\text{ISM}} + \text{DM}_{\text{CGM}} + \text{DM}_{\text{IGM}} + \text{DM}_{\text{host}}, \quad (2)$$

where in this formulation DM_{ISM} includes the warm ionized medium (WIM) in the Milky Way disk (e.g., Cordes & Lazio 2002; Yao et al. 2017), DM_{CGM} is the DM contributed by the Galactic CGM, DM_{host} is the DM associated with the FRB host-galaxy interstellar medium (ISM) and their halos, and DM_{IGM} includes contributions from the intergalactic medium (IGM) and any intervening galaxy systems. For pulsars within the Milky

Way halo, such as in the Magellanic Clouds and in several globular clusters, $DM_{\text{IGM}} = 0 \text{ pc cm}^{-3}$. These expressions apply to the redshift ~ 0 regime relevant to this paper. If the components of DM_{obs} can be accurately modeled or bounded, constraints can be placed on DM_{CGM} . Modeling of the DMs of pulsars in the LMC led [Anderson & Bregman \(2010\)](#) to find a very low $M_{\text{CGM}} \sim 1.5 \times 10^{10} M_{\odot}$ assuming a [Navarro et al. \(1997\)](#) profile (an NFW profile); it is likely that an overly large DM_{ISM} was assumed, and the NFW profile is no longer favored for the Galactic CGM. Although most FRBs are too distant to allow for accurate modeling of the components of DM_{obs} , FRBs from nearby galaxies ([Bhardwaj et al. 2021](#); [Kirsten et al. 2022](#)) have begun to be used to place constraints on DM_{CGM} , assuming specific models for DM_{ISM} , that are in tension with some models for the Milky Way CGM.

In this paper we present observations with the Deep Synoptic Array (DSA-110) of a new FRB (FRB 20220319D) that motivates stringent new constraints on the mass of the Milky Way CGM. Remarkably, FRB 20220319D was observed to have $DM_{\text{obs}} < DM_{\text{ISM}}$ for leading models of the warm-gas distribution in the Galactic disk, despite the unambiguous association we find with a galaxy at a distance of 50 Mpc. We detail observations of the FRB in §2. We consider the association with its host galaxy in §3, wherein we show that the DM of FRB 20220319D is consistent with an extragalactic origin given uncertainties in models for DM_{ISM} , using observations of the DMs of pulsars in globular clusters with accurate parallax distances. We present an analysis of the host environment of FRB 20220319D in §4. We then place conservative constraints on DM_{CGM} , and hence M_{CGM} , using FRB 20220319D and the distant high-latitude globular cluster M53, in §5. We discuss the implications of our results in §6, and conclude in §7.

2. DSA-110 OBSERVATION OF FRB 20220319D

The DSA-110¹ is a radio interferometer hosted at the Owens Valley Radio Observatory (OVRO), purpose built for the discovery and arcsecond-localization of FRBs. A full description of the instrument will be presented in [Ravi et al. \(in prep.\)](#). During the observations discussed herein, the DSA-110 was configured as described in [Ravi et al. \(2022\)](#). Of particular note is that when FRB 20220319D was observed, early in DSA-110 commissioning, all candidates at DMs in excess of

¹ <https://deepsynoptic.org>

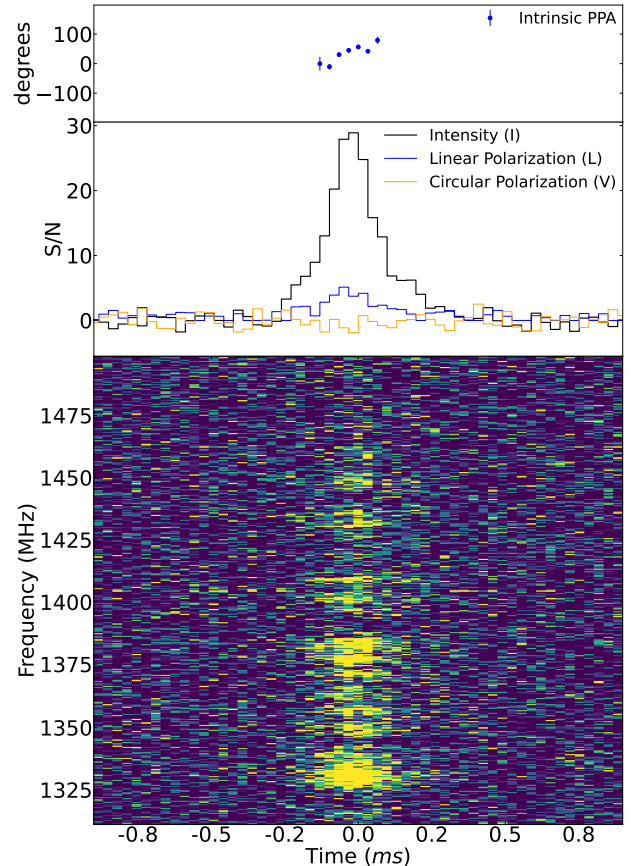


Figure 1. Dedispersed temporal profile and dynamic spectrum of FRB 20220319D. A value of $DM_{\text{obs}} = 110.95 \text{ pc cm}^{-3}$ was used. The top panel shows the estimated absolute position angle based on an approximate parallactic angle, the $\sim 20^\circ$ error due to RM uncertainty is not included in the error bars. The middle panel shows temporal profiles in total intensity, linearly polarized intensity, and Stokes V, as labeled. The bottom panel shows the dynamic spectrum of the total-intensity data. The time resolution in the time-series and dynamic-spectrum plots is $32.768 \mu\text{s}$, and the temporal profile is in units of signal to noise ratio. The reference time is MJD 59657.93275696795, which was the burst arrival time at OVRO at 1530 MHz. The polarized data on the burst was corrected for the measured RM of 50 rad m^{-2} .

80 pc cm^{-3} were saved for further inspection, regardless of the expected DM through the Galactic disk.

FRB 20220319D was detected during standard commissioning observations, with an arrival time at OVRO at 1530 MHz of MJD 59657.93275696795. During these observations, the DSA-110 was parked at a pointing-center declination of $+71.6^\circ$. The DSA-110 reference position is -118.283° longitude, $+37.2334^\circ$ latitude. FRB 20220319D was detected with a DM of $110.96 \text{ pc cm}^{-3}$, and a signal to noise ratio (S/N) of 41.7. To derive optimized burst parameters and polarization properties, we coherently combined voltage data from

the 48 core antennas towards the detection-beam direction. The resulting temporal profile and calibrated dynamic spectrum, produced with incoherent dedispersion at the native time and frequency resolutions, are shown in Figure 1, and optimized parameters are given in Table 1. The polarization analysis was done following procedures described in Ravi et al. (2022). The matched-filter total-intensity S/N estimate is 79.

The burst exhibits a narrow temporal profile with a strongly modulated spectrum. The DM smearing timescale ranges between 8–13 μs within the DSA-110 band, and so the data resolve the temporal structure of the burst. Scaling the system-equivalent flux density of the DSA-110 by the primary-beam attenuation at the burst position, we derive a fluence of 11.2 ± 0.2 Jy ms. Following techniques described in Connor et al. (2020), we derive a spectral decorrelation bandwidth, $\nu_d = 3.6 \pm 0.2$ MHz, defined as the $1/e$ scale of the autocorrelation function of the spectrum. The burst spectro-temporal morphology is consistent with the population of so far non-repeating FRBs (Pleunis et al. 2021). We derive a low fractional polarization of just 16% (Figure 1), with no significant circular polarization. A Faraday rotation measure (RM) of 50 ± 15 rad m^{-2} was detected. The error was estimated by simulating the recovery of RMs with the same linear-polarization S/N as FRB 20220319D (Sherman et al., in prep.).

The interferometric localization of FRB 20220319D was derived following procedures largely described in Ravi et al. (2022). Correlation products for all baselines formed from the 63 functioning antennas of the DSA-110 at the time of detection were integrated over 262.144 μs centered on the burst arrival time. Bandpass calibration was done using a 10-min observation of 3C309.1 observed 11 hr prior to the burst detection. Complex gain calibration at the time of the burst detection was derived using an NRAO VLA Sky Survey (NVSS; Condon et al. 1998) model and 5 min of visibility data. We show images of the point-spread function (PSF; a flat spectrum was assumed), and the pre- and post-deconvolution images of FRB 20220319D in Figure 2. Briggs weighting with a ‘robust’ parameter of 0.5 was used to suppress sidelobes, given the high S/N of FRB 20220319D, yielding a PSF FWHM of $26.9'' \times 15.6''$. The position of FRB 20220319D, given in Table 1, was derived by fitting an elliptical Gaussian to the deconvolved image of FRB 20220319D.

We derived the uncertainty in the FRB position using data on nine compact bright sources from the Radio Fundamental Catalog (RFC; rfc_2022c), obtained within 2 hr of the burst observation. A fit to a linear trend in R.A. and Decl. was used to derive arcsecond-level astro-

Table 1. Properties of FRB 20220319D.

Parameter	Value
Arrival time (MJD) ^a	59657.93275696795
DM (pc cm^{-3})	110.95(1)
Full-width half-maximum (ms)	0.16(1)
Fluence (Jy ms)	11.2(2)
Spectral energy (erg Hz^{-1})	$3.3(1) \times 10^{28}$
L/I ^b	0.16(3)
$ V/I $ ^b	0.04(3)
RM (rad m^{-2})	50(15)
ν_d (MHz) ^c	3.6(2)
R.A. (J2000)	02:08:42.7(1)
Decl. (J2000)	+71:02:06.9(6)

^a Arrival time at OVRO at 1530 MHz.

^b L/I is the fraction of linearly polarized fluence, and $|V/I|$ is the absolute value of the fraction of circularly polarized fluence.

^c ν_d is the characteristic spectral decorrelation bandwidth.

metric corrections, and the corresponding uncertainties. These uncertainties (0.52'' in R.A. and 0.5'' in Decl.) were then added in quadrature to the statistical uncertainty in the fitted burst position (0.29'' in R.A. and 0.17'' in Decl.) to derive a final 90% confidence containment ellipse with semi-axes of 1.25'' in R.A. and 1.18'' in Decl. This ellipse is shown in the bottom-left panel of Figure 2, together with the detrended position offsets of the RFC sources. We also assessed the quality of the in-field calibration by checking the positions of bright (> 50 mJy) compact ($< 20''$) NVSS sources within the primary-beam FWHM against NVSS catalog positions. These offsets (with the RFC corrections applied) are also shown in Figure 2. A more detailed analysis of the DSA-110 localization accuracy will be presented in Ravi et al. (in prep.).

3. ASSOCIATION WITH IRAS 02044+7048, AND UNCERTAINTIES IN DM_{ISM}

The 90% confidence localization region of FRB 20220319D is shown in Figure 3 overlaid on a Pan-STARRS1 (PS1) i -band image. The galaxy coincident with the FRB location is cataloged in the NASA Extragalactic Database as IRAS 02044+7048, with a spectroscopic redshift of 0.011 indicating a distance of approximately 50 Mpc. Using observations described below, we derive a spectroscopic redshift of

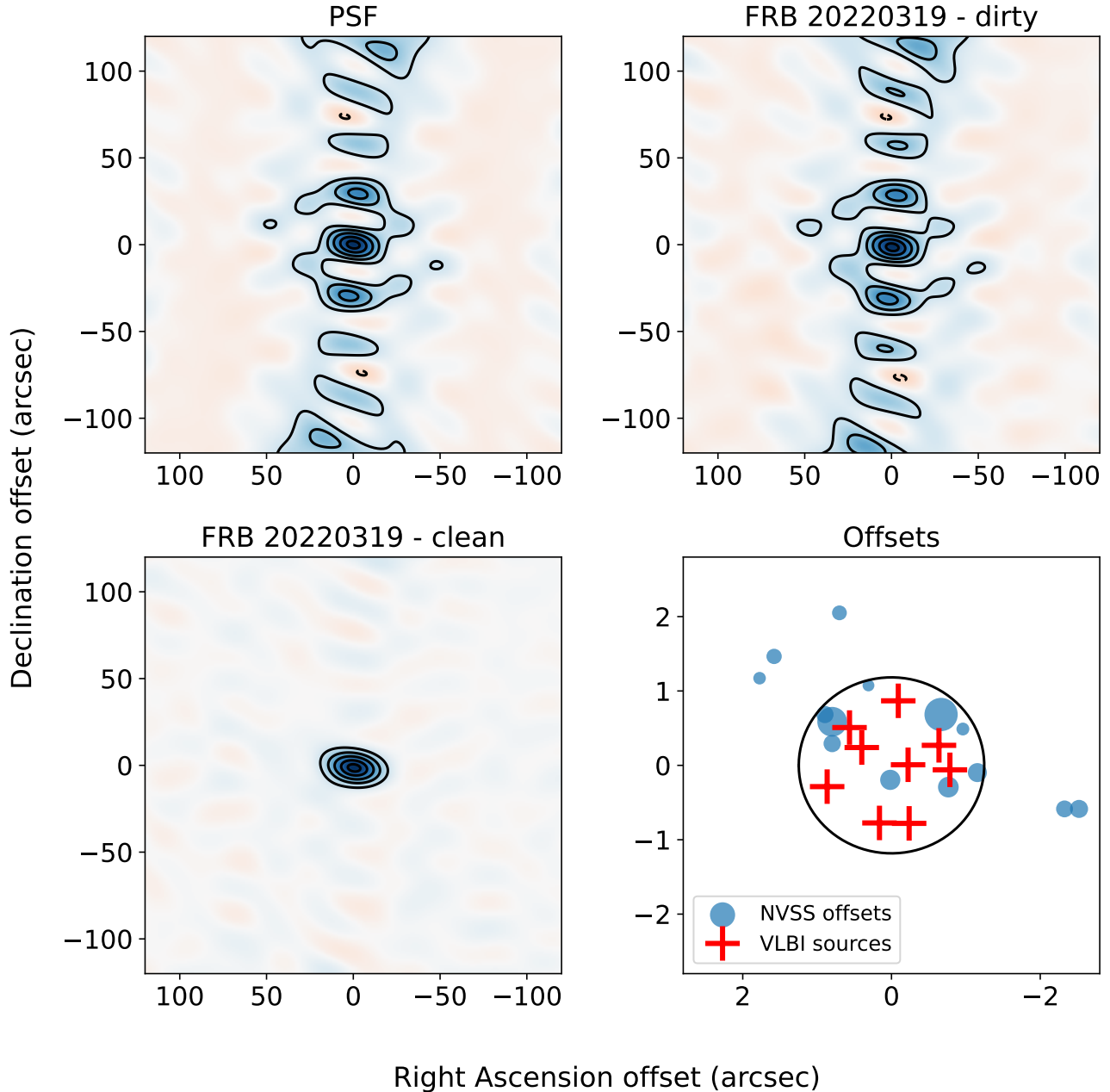


Figure 2. DSA-110 localization of FRB 20220319D. *Top left:* Point-spread function (PSF) of the DSA-110 for the observation of FRB 20220319D, assuming a flat-spectrum source. *Top right:* Dirty image of FRB 20220319D, with no deconvolution applied. *Bottom left:* Deconvolved image of FRB 20220319D. The synthesized beam is represented by an ellipse with half-power diameters of $26.9'' \times 15.6''$, at a position angle of 80° . Briggs weighting was used with a ‘robust’ parameter of 0.5, in order to partially suppress PSF sidelobes. Baselines shorter than 200λ were excluded from the analysis because they were affected by spurious cross-coupling. Contours in the preceding three panels are at -0.4 , -0.2 (dashed), 0.2 , 0.4 , 0.6 , 0.8 and 0.9 (solid) of the peak intensity. The images are centered on the coordinates (R.A. J2000, decl. J2000) = (02:08:42.7, +71:02:06.9). *Bottom right:* Offsets of known astronomical sources from their true positions as measured by the DSA-110. The blue disks show offsets of sources from cataloged positions in the NRAO VLA Sky Survey (NVSS; Condon et al. 1998) in a 5 min DSA-110 image formed from data taken at a time centered on the burst detection. Only sources with cataloged flux densities > 50 mJy and measured major-axis diameters $< 20''$, within 2 deg of the pointing center, were considered. The symbol size is proportional to flux density. The red crosses show measured offsets of nine RFC calibrator sources (see text for details) observed immediately preceding and after the burst. The ellipse indicates the 90% confidence containment region for FRB 20220319D, derived from the RFC calibrators.

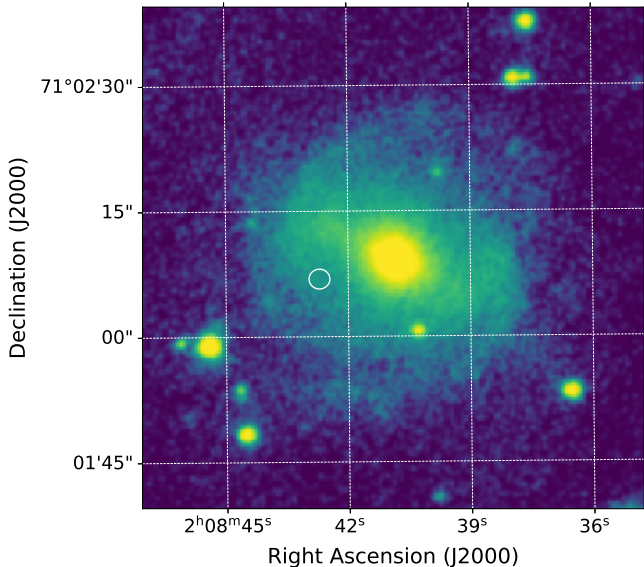


Figure 3. Pan-STARRS *i*-band image of IRAS 02044+7048, with the 3.7×2.2 arcsec 90% confidence localization region of FRB 20220319D indicated as a white ellipse.

0.0111 ± 0.0004 , indicating a luminosity distance of 49.6 Mpc. An isophotal fit to the PS1 *i*-band image indicates an effective radius of 2.7 ± 0.2 kpc, and the FRB is offset by 2.3 ± 0.3 kpc. The isophotal analysis also indicates an inclination of 23 ± 3 deg. A barred spiral morphology, with a classification of SBa, is evident from the image.

Under the assumption that FRB 20220319D is extragalactic, the spatial association between FRB 20220319D and IRAS 02044+7048 is secure. It is unlikely that FRB 20220319D lies significantly beyond IRAS 02044+7048; the morphology of the galaxy indicates the presence of a warm-ISM phase, and scattering in this ISM would likely cause temporal broadening of several hundred milliseconds at our observing frequencies (Cordes et al. 2022; Ocker et al. 2022). The Gravitational Wave Galaxy Catalog (GWGC; White et al. 2011) lists 15869 galaxies at distances less than 50 Mpc, subtending a total of 4 deg^2 . Thus the chance-association probability of FRB 20220319D and a galaxy at < 50 Mpc is $\lesssim 10^{-4}$.

The extragalactic nature of FRB 20220319D is called into question by its DM of $110.95 \text{ pc cm}^{-3}$. The predicted DM for extragalactic objects along its $l = 129.2^\circ$, $b = +9.1^\circ$ sightline is 132.9 pc cm^{-3} according to the NE2001 model for the Galactic ionized ISM distribution (Cordes & Lazio 2002), and 187.7 pc cm^{-3} according to the YMW16 model (Yao et al. 2017). The RM detection for FRB 20220319D of $50 \pm 15 \text{ rad m}^{-2}$ is, however, marginally consistent with being in excess of the

expected Milky Way contribution along the burst sightline. A recent model for the Galactic RM foreground along this sightline (Hutschenreuter et al. 2022) indicates an expected Galactic RM of $-14 \pm 18 \text{ rad m}^{-2}$ towards FRB 20220319D. We cannot draw conclusions from the measured spectral decorrelation bandwidth of $\nu_d = 3.6 \pm 0.2$ MHz, which is far in excess of the 0.2 MHz decorrelation bandwidth predicted by NE2001 due to scattering in the Milky Way ISM, because the origins of the spectral structure cannot easily be determined.

We now analyze the performance of the NE2001 and YMW16 models with the aim of determining whether the model uncertainties can accommodate an extragalactic origin for FRB 20220319D. Both model the distribution of the WIM (Draine 2011) in the Galactic disk using observations of radio-wave propagation, with a dominant thick-disk component encapsulating several overdensities and voids motivated by multiwavelength data. The YMW16 model is fit to pulsars with independent DM and distance estimates, whereas the NE2001 model is additionally fit to pulsar and extragalactic radio-source scattering measurements. For low-latitude extragalactic sightlines, the radial extent of the thick disk is critical in determining DM_{ISM} . In NE2001, a cutoff at a radius of 20 kpc is motivated by observations of HII regions in other galaxies and scattering of extragalactic sources. Surveys of Galactic HII regions on the other hand motivate the cutoff of 15 kpc in YMW16. Neither cutoff is estimated in the NE2001 or YMW16 fits; rather they are fixed model choices that do not impact the match between the models and the data under consideration. The functional forms for the WIM distribution in the thick disk also differ, with NE2001 incorporating an oblate spheroid, and YMW16 incorporating a plane-parallel slab that results in significant deviations from NE2001 at low latitudes in the second and third quadrants (e.g., Price et al. 2021). High-latitude extragalactic sightlines are likely to be better modeled because the scale height of the thick disk is a critical fitted parameter. However, density fluctuations caused by turbulence in the WIM, together with clumps and voids, complicate our picture even at high latitudes (Ocker et al. 2020). Large-scale WIM inhomogeneities at the disk-halo interface such as Galactic chimneys (e.g., Koo et al. 1992; Normandeau et al. 1996) can result in significant departures from spatially smooth models for DM_{ISM} .

We first note that the recent PSR π sample of pulsar parallax measurements (Deller et al. 2019) reveals discrepancies between the NE2001 and YMW16 models and measured pulsar distances at low latitudes in the second quadrant, where FRB 20220319D appears on the sky. In general, known errors in NE2001 and YMW16

exhibit significant spatial correlation (e.g., [Price et al. 2021](#)), motivating the consideration of sources along sightlines similar to FRB 20220319D. Table 2 lists the DMs of the three nearest pulsars in the sample to FRB 20220319D, together with the predicted DMs given the measured distances. The YMW16 model significantly overpredicts all three DMs, and although NE2001 is more accurate for the modestly distant pulsars likely in the Cygnus-Orion arm, it also overpredicts the DM of the more distant PSR J0406+6138.

A more detailed analysis of the performance of the models for sightlines towards distant objects is enabled by the recent convergence in the distances to globular clusters hosting pulsars. We obtain accurate distance estimates (less than few-percent errors) to all 21 globular clusters with associated pulsars ([Manchester et al. 2005](#)) at $|b| > 5^\circ$ from the compilation of [Baumgardt & Vasiliev \(2021\)](#), primarily based on *Gaia* parallaxes ([Vasiliev & Baumgardt 2021](#)). Clusters at lower latitudes are not considered because their DMs are influenced by the thin disk and other components in the Galactic plane. For each cluster we compare the difference between the DMs predicted by the NE2001 and YMW16 models for the cluster distances, and the true cluster DMs defined as the mean DMs of the associated pulsars. The results are shown in Figure 4; FRB 20220319D is also included with the predicted DM set to DM_{ISM} . The errors in NE2001 at low latitudes can clearly accommodate an extragalactic origin for FRB 20220319D. YMW16 generally performs better than NE2001 for the low-latitude clusters, but these are nearly all in the first and fourth quadrants (with NGC 1851 as the only exception), and so perhaps not representative of errors along sightlines closer to the Galactic anticenter.

As an additional check of the Galactic sightline towards FRB 20220319D, we also consider independent measures of DM_{ISM} . First, we use the relation between the neutral hydrogen column density and pulsar DMs derived by [He et al. \(2013\)](#) to estimate the DMs towards FRB 20220319D and each globular cluster, assuming no HI gas beyond the clusters. We obtain HI column densities from the HI4PI data ([HI4PI Collaboration et al. 2016](#)). The results are shown in Figure 4, including errors representing intrinsic scatter in the relation. The HI column densities result in underestimates of the DMs towards low-latitude clusters, possibly reflecting the increased ionization of HI gas towards the central regions of the Galaxy (e.g., [Madsen & Reynolds 2005](#)). The HI-predicted DM_{ISM} for FRB 20220319D

is consistent with an extragalactic origin, although the uncertainties are large. Second, we estimate the DMs towards FRB 20220319D and each globular cluster using $\text{H}\alpha$ emission measures (EMs) derived from the Wisconsin $\text{H}\alpha$ Mapper (WHAM) all sky maps ([Haffner et al. 2003](#)). We follow the analysis of [Berkhuijsen et al. \(2006\)](#), wherein the photon fluxes, $F_{\text{H}\alpha}$ (in units of Rayleighs), integrated over the range of Galactic velocities are converted to DMs using the following relations:

$$\text{EM} = 2.25 F_{\text{H}\alpha} e^{2.2E(B-V)} \text{ cm}^{-6} \text{ pc} \quad (3)$$

$$\text{DM} = (\text{EM} \times D \times \mathcal{F})^{1/2}. \quad (4)$$

$$\mathcal{F} = \frac{f}{\zeta(1 + \epsilon^2)} \quad (5)$$

The expression for \mathcal{F} (e.g., [Ocker et al. 2020](#), and references therein) encodes an ionized clouddlet model, wherein the WIM is composed of clouddlets with a volume filling factor f , $\zeta = \langle n_e^2 \rangle / \langle n_e \rangle^2 \sim 2$ captures the cloud to cloud variation, and $\epsilon^2 \lesssim 1$ is the density variance internal to the clouddlets. Further, $E(B - V)$ is a measure of the interstellar reddening along a given sightline, and D is the distance through the WIM. We have assumed a uniform WIM electron temperature of 8000 K, and equivalence between the line-of-sight and volume filling factors. We find that for the cluster sightlines the $\text{H}\alpha$ -based DM estimates perform remarkably well for a nominal value $\mathcal{F} = 0.1$ (i.e., $f \gtrsim 0.4$), comparably to YMW16 and better than NE2001 for low-latitude sightlines. This is surprising given previous results for pulsar DMs (e.g., [Schnitzeler 2012](#)), but may be explained by globular clusters generally lying beyond the outer extent of the WIM, obviating the need for distance corrections to the WHAM EMs. For the FRB 20220319D sightline, the $\text{H}\alpha$ flux implies $\text{DM}_{\text{ISM}} = 89 \text{ pc cm}^{-3}$, which is 22 pc cm^{-3} lower than the measured DM.

We conclude that models for the DM towards FRB 20220319D contributed by the Galactic WIM are consistent with an extragalactic origin. This secures the association of the burst with the galaxy IRAS 02044+7048. Consistent with the original presentations of the NE2001 and YMW16 models for the WIM distribution, we confirm that there are significant model uncertainties at low Galactic latitudes. We used a large sample of globular-cluster parallax distances, which have DM estimates from associated pulsars, to demonstrate that an alternative predictor of DM_{ISM} based on the total Galactic $\text{H}\alpha$ flux can provide a useful check on the aforementioned models. In order to estimate DM_{ISM} towards FRB 20220319D we consider pulsars that are nearby on the sky and at a similar Galactic latitude. The two nearest pulsars within 1 deg of the burst in Galactic latitude, PSR J0231+7026 (total separation of 1.9 deg)

Table 2. Measured and predicted DMs of PSR π pulsars near FRB 20220319D.

Pulsar	l (deg.)	b (deg.)	FRB offset (deg)	Distance (kpc)	DM ^a	NE2001 ^a	YMW16 ^a
PSR J0147+5922	130.1	-2.7	12	$2.02^{+0.46}_{-0.16}$	40.1	31.8	79.0
PSR J0157+6212	130.6	0.3	9	$1.80^{+0.08}_{-0.12}$	30.2	31.5	59.3
PSR J0406+6138	144.0	7.0	15	$4.58^{+1.63}_{-0.87}$	65.3	123.7	141.7

^aAll DMs are given in units of pc cm^{-3} .

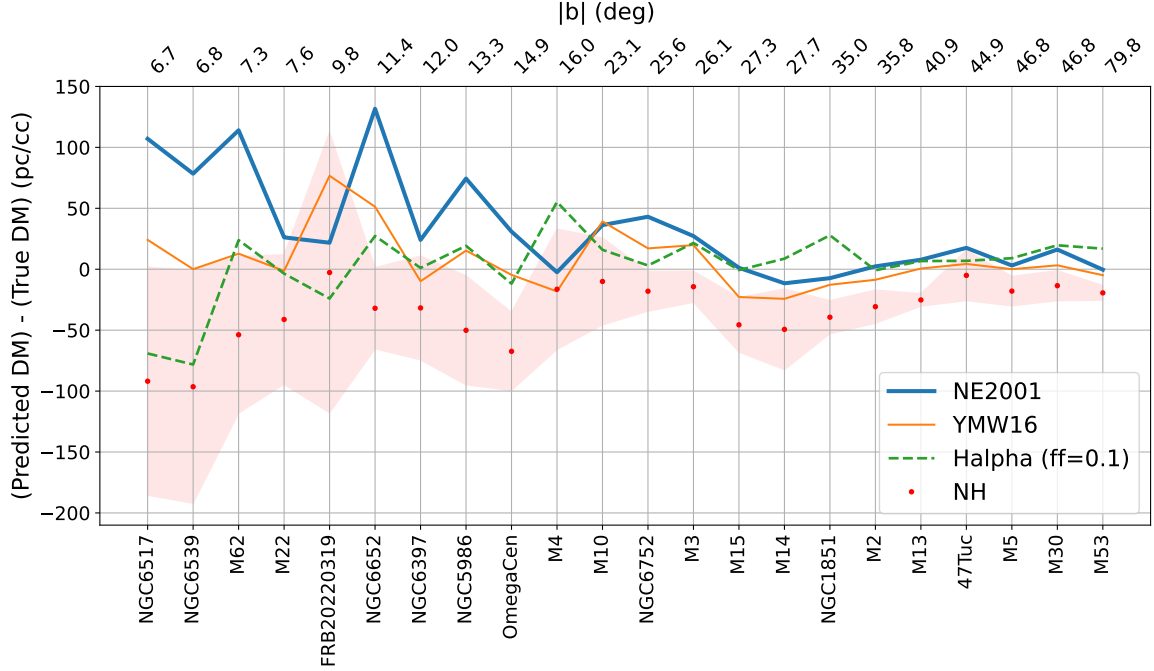


Figure 4. Difference between the predicted DM and true DM of all globular clusters that host pulsars, sorted by increasing $|b|$. Predictions are made for each globular cluster given its distance and location on the sky, using four different models for the warm ISM of the Milky Way. The two literature models are NE2001 (blue solid thick curve) and YMW16 (orange solid thin curve). We also convert the measured H α emission measures (green dashed curve) and HI columns (red dots and shaded region) along each sightline to DM predictions using methods described in the text. We also include predictions for FRB 20220319D assuming a location beyond the Galactic disk.

and PSR J0325+6744 (total separation of 7.4 deg), have DMs of 46.7 pc cm^{-3} and 65.3 pc cm^{-3} , and we consider these as conservative and less conservative estimates respectively of DM_{ISM} along the burst sightline. We note that the predicted NE2001 and YMW16 DM_{ISM} values along the sightlines towards these pulsars are lower than along the burst sightline.

4. THE HOST ENVIRONMENT OF FRB 20220319D

We obtained long-slit optical spectroscopy of IRAS 02044+7048 using the Double Spectrograph (DBSP; Oke & Gunn 1982) mounted on the Palomar 200-inch Hale telescope on 2022 June 01 (UT).

The observations were undertaken under conditions of $1.2''$ seeing, at an airmass of 1.9, and used a $1.5''$ slit positioned to include both the FRB location and the galaxy nucleus at a position angle of 104° . Two 600 s exposures were obtained with the D55 dichroic and the 316/7500 grating on the red arm; we only considered data from the red arm of the spectrograph given the significant extinction along this sightline ($A_V = 2.209$; Schlafly & Finkbeiner 2011). The two-dimensional spectral data were reduced according to standard procedures using a PyPeIt-based pipeline (Prochaska et al. 2020). We then defined the trace function using observations of the standard star Feige 34, and extracted spectra in $1.5''$ windows along the slit. Feige 34 was also used

Table 3. Observed and derived parameters of the host galaxy of FRB 20220319D, IRAS 02044+7048. 1σ errors in the last significant figures are given in parentheses.

Parameter	Value
Redshift	0.0111(4)
Luminosity distance (Mpc)	49.6
Effective radius (kpc)	2.7(2)
FRB projected offset (kpc)	2.3(3)
$\log M_*$ (M_\odot)	9.93(7)
$\log Z^a$	0.1(0.2)
Internal A_V^b	$0.2^{+0.2}_{-0.1}$
SFR ($M_\odot \text{ yr}^{-1}$) ^c	1.8(0.7)
Inclination (deg)	23(3)

^aMetallicity with respect to solar.

^bV-band extinction corresponding to a uniform dust slab.

^cAveraged over the past 100 Myr.

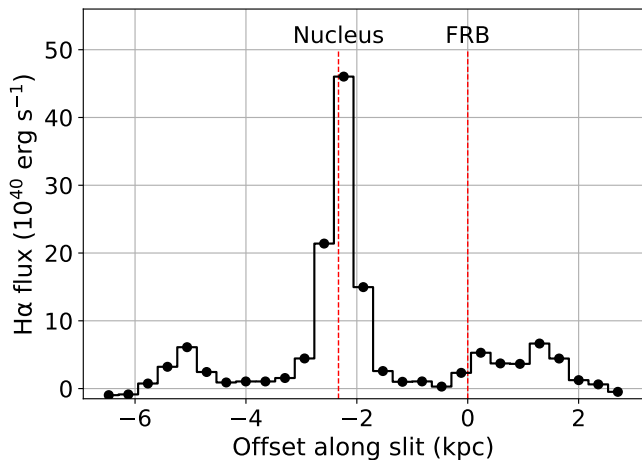


Figure 5. Total $H\alpha$ flux observed at different locations within our longslit spectroscopic observations of IRAS 02044+7048. Measurements were obtained at $1.5''$ intervals along a $1.5''$ longslit oriented at a position angle of 104° , which covered both the FRB position and the center of the galaxy. The locations of the galaxy nucleus and FRB 20220319D are indicated in the figure.

for flux calibration, and all spectra were corrected for extinction according to the Fitzpatrick & Massa (2007) extinction curve.

We detected $H\alpha$ emission at several locations along the slit, as shown in Figure 5. The strongest $H\alpha$ emission is observed at the galaxy core, from which we also detect

lines corresponding to [NII] and [SII]. These lines were together used to derive a redshift of 0.0111 ± 0.0004 for IRAS 02044+7048. Although we do not detect $H\beta$ or [OIII], the ratio $\log [\text{NII}]/H\alpha = -0.23 \pm 0.02$ indicates a $< 10\%$ chance of the nuclear ionization being purely due to star formation activity (Ho et al. 1997; Kewley et al. 2006). There is evidence of $H\alpha$ emission from spiral-arm features on either side of the nucleus; these features are too extended to represent HII regions. The FRB appears associated with the eastern arm, although not at the center of its $H\alpha$ radial profile. No additional evidence for or against an arm association can be gleaned from the residuals of a fit of the IRAS 02044+7048 image in Figure 3 to a two-dimensional Sersic profile.

In order to determine global properties of IRAS 02044+7048, we derived and modeled its spectral energy distribution (SED). We executed aperture photometry on archival images from the Panoramic Survey Telescope and Rapid Response System (Pan-STARRS; Chambers et al. 2016), Two Micron All Sky Survey (2MASS; Skrutskie et al. 2006), and ALLWISE (Cutri et al. 2021) surveys. We identified an elliptical aperture that captured the i -band extent of the galaxy in Pan-STARRS data, and masked likely foreground objects. We then used this aperture, convolved with the PSF of each survey, to measure extinction-corrected AB magnitudes in all filters used by Pan-STARRS, 2MASS, and WISE. We modeled this SED using the Prospector stellar population synthesis modeling code (Johnson et al. 2021). We ran Prospector using recommended techniques and priors and a non-parametric star-formation history (SFH) model (Leja et al. 2019), and sampled from the posterior using emcee (Foreman-Mackey et al. 2013). Non-parametric models for the SFH result in less bias in both stellar-mass (M_*) and star-formation rate (SFR) estimates, because specific SFH models are not excluded a priori. We included a model for dust re-radiation in the likelihood function. The spectral energy distribution of IRAS 02044+7048 is shown in Figure 6, together with the results from the Prospector analysis, and derived maximum a posteriori probability parameters are listed in Table 3. The SFR of $1.8 M_\odot \text{ yr}^{-1}$ was derived by integrating the SFH over the past 100 Myr.

IRAS 02044+7048, and the location of FRB 20220319D within it, are largely consistent with previous results on FRB host galaxies and environments (Bhandari et al. 2020; Heintz et al. 2020; Bochenek et al. 2021; Mannings et al. 2021; Bhandari et al. 2022). Most FRB host galaxies have detectable ongoing star formation, and some exhibit signatures of additional nuclear ionization sources. The stellar mass of IRAS 02044+7048 is entirely consistent with the distri-

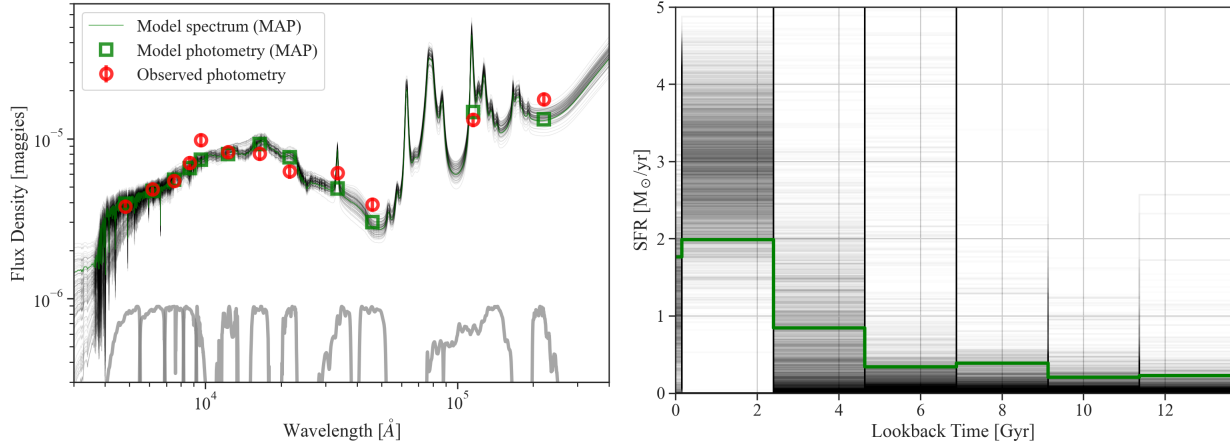


Figure 6. *Left:* Prospector fit to the spectral energy distribution (SED) of the host galaxy of FRB 20220319D, IRAS 02044+7048. The SED measurements from archival PanSTARRS, 2MASS, and WISE data are shown in red, together with representative 10% errors. Filter transmission curves are shown in grey. The maximum a posteriori probability (MAP) model photometry is shown in green, together with the MAP spectrum. 100 spectra generated using random draws from the posterior distributions of the model parameters are shown in black. *Right:* Measured SFH of IRAS 02044+7048 (green). The results from 100 random draws from the posterior distributions are shown in black.

bution of masses found for both repeating and so far non-repeating FRB hosts. The potential association of FRB 20220319D with a spiral-arm feature is consistent with the results of Mannings et al. (2021) based on Hubble Space Telescope imaging of eight FRB hosts. In the absence of very long baseline interferometry, our data do not have sufficient angular resolution to determine whether or not the FRB originates from within an association of young stars (e.g., Tendulkar et al. 2021). The location of FRB 20220319D at an offset of $\sim 85\%$ of the effective radius from the galaxy nucleus is consistent with the range of previously observed FRB offsets.

However, the SFR of IRAS 02044+7048 is rather high for its stellar mass, with respect to the observed sample of hosts of so far non-repeating FRBs (Bhandari et al. 2022). Only one so far non-repeating FRB (20190102C, at $z = 0.2912$) has a comparably high specific SFR (sSFR), of $\log \text{sSFR} = -9.74$. Although IRAS 02044+7048 is consistent with a location on the star-forming main sequence of galaxies (Speagle et al. 2014), non-repeating FRB hosts as a population are consistent with originating from below this sequence. It is possible that FRBs from more actively star-forming hosts are selected against in existing radio surveys due to propagation effects in the host ISM (Seebeck et al. 2021), in which case it is not surprising that IRAS 02044+7048 has a face-on orientation.

5. THE MASS OF THE MILKY WAY CGM

The constraints on the extragalactic DM contribution along the sightline towards FRB 20220319D are severe. Adopting the two estimates discussed above for DM_{ISM} from pulsars nearby to the FRB on the sky, we find

possible upper limits on the extragalactic DM contribution ($\text{DM}_{\text{CGM}} + \text{DM}_{\text{IGM}} + \text{DM}_{\text{host}}$) of either 45.7 pc cm^{-3} or 64.3 pc cm^{-3} . Even with our conservative estimates for DM_{ISM} , FRB 20220319D has the lowest extragalactic DM yet measured for an FRB localized to a host galaxy. We thus have the opportunity to stringently bound the heretofore poorly constrained value of DM_{CGM} , and thus directly bound the mass of the Galactic CGM. The IGM likely contributes 7 pc cm^{-3} towards IRAS 02044+7048, assuming an IGM baryon fraction of 0.7 (e.g., Macquart et al. 2020). The detection of extended $\text{H}\alpha$ emission from the galaxy itself, and in particular at the location of FRB 20220319D, indicates that the WIM component of the ISM is present, although we do not know where within the ISM column the FRB source is located.² We simply assume a nominal value of $\text{DM}_{\text{host}} = 10 \text{ pc cm}^{-3}$ for our analysis below. Thus, we find that for the FRB 20220319D sightline, two possible upper limits on DM_{CGM} are 28.7 pc cm^{-3} and 47.3 pc cm^{-3} , depending on the assumption for DM_{ISM} . These upper limits are comparable to previous results from the closest known FRB source (FRB 20200120E), in a globular cluster associated with M81, which provide possible upper limits on DM_{CGM} of 32 pc cm^{-3} and 42 pc cm^{-3} depending on the choice of NE2001 or YMW16 for DM_{ISM} (Kirsten et al. 2022). The constraints from FRB 20200120E are affected by a reliance on the NE2001/YMW16 models for

² With a measurement of scattering in the host ISM, it is possible to estimate DM_{host} (Cordes et al. 2022). However, upper limits on the temporal broadening of FRB 20220319D of $\sim 0.1 \text{ ms}$ are not usefully constraining.

DM_{ISM}, and by stronger assumptions for the halo DM of M81.

A recent synthesis of models for the Galactic CGM DM by Keating & Pen (2020) highlighted the wide range of extant predictions. In this work, we use a representative set of models to demonstrate the implications of the constraint on DM_{CGM} from FRB 20220319D. The models are illustrated in Figure 7. We also consider measurements of the DM contributed by sightlines through the halo from pulsars in the LMC (Ridley et al. 2013) and in the distant (18.5 kpc; Baumgardt & Vasiliev 2021) globular cluster M53 (Kulkarni et al. 1991; Pan et al. 2021). Although the LMC is at $b \approx -33^\circ$ and M53 is at $b \approx +80^\circ$, we conservatively subtract the lowest DM_{ISM} to be found in either the NE2001 or YMW16 models of 18 pc cm^{-3} to estimate the halo DM contributions along their sightlines. In the top two panels of Figure 7, we show the resulting upper limits on DM_{CGM} towards M53 and the LMC, with ranges corresponding to the range of associated pulsar DMs. The bottom-left panel shows the upper limit on DM_{CGM} from FRB 20220319D, placed at the virial radius of the Milky Way halo. In all cases we show model predictions for DM_{CGM} assuming a spherically symmetric galactocentric baryon halo, but with the DM evaluated along sightlines from the position of the Earth (GRAVITY Collaboration et al. 2019). We evaluate the modified NFW (mNFW) and Maller & Bullock (2004) profiles following Prochaska & Zheng (2019), with a total Milky Way mass of $M_{\text{tot}} = 1.5 \times 10^{12} M_\odot$, and a halo baryon fraction of $f_{\text{CGM}} = 0.75$. The Pen (1999) model is evaluated for the same M_{tot} and with the core radius set to the halo virial radius. The semi-empirical Miller & Bregman (2013) and Faerman et al. (2017) models and the semi-analytic Faerman et al. (2020) model are all evaluated as given. Finally, in the bottom-right panel of Figure 7, we also show the model predictions for the halo baryon density along the LMC sightline, together with constraints from ram-pressure stripping analyses of dwarf galaxies (Salem et al. 2015; Putman et al. 2021) and modeling of OVII and OVIII emission measurements (Kaaret et al. 2020).

The data are in favor of models that predict lower total CGM DMs and lower inner densities (e.g., Pen 1999; Faerman et al. 2020; Miller & Bregman 2013). The DMs of M53 pulsars and FRB 20220319D deliver consistent constraints on the range of models, albeit on very different radial distance scales. The constraints from LMC pulsars are less impactful, but nonetheless also exclude the three models (Maller & Bullock 2004; Faerman et al. 2017; Prochaska & Zheng 2019) considered here that predict larger values of DM_{CGM}. We note that our treatment of the CGM contribution to the DMs of LMC pul-

sars is far more conservative than that of Anderson & Bregman (2010); this is motivated by the uncertainties discussed above in estimating DM_{ISM}. The DM constraints are consistent with the most robust density estimates that we consider (Salem et al. 2015; Kaaret et al. 2020). The density estimates are however subject to the uncertainties discussed in §1, and we proceed by considering only the constraints on DM_{CGM}.

We now derive constraints on the mass of the Galactic CGM, M_{CGM} , by finding β models that are consistent with the FRB 20220319D and M53 DMs. When converting the electron column density to a mass column density, we assume 1.18 proton masses per electron following Yamasaki & Totani (2020), which corresponds to roughly solar metallicity gas. The β profile is widely adopted in the field to convert (column-)density estimates to halo masses (e.g., Miller & Bregman 2013; Salem et al. 2015; Kaaret et al. 2020), as it is empirically motivated. The electron number density at a radius r is given by

$$n(r) = n_0 \left[1 + \left(\frac{r}{r_c} \right)^2 \right]^{-3\beta/2}, \quad (6)$$

where n_0 is a central density, and r_c is a core radius that we fix to 0.47 kpc following Miller & Bregman (2013). The exact value of the core radius is unimportant for our conclusions regarding M_{CGM} . Typical values of β found using various CGM tracers are in the range $0.4 \lesssim \beta \lesssim 0.5$ (e.g., Miller & Bregman 2013, 2015; Salem et al. 2015; Kaaret et al. 2020). We consider three constraints on DM_{CGM}: the lower and upper constraints from FRB 20220319D, and the lower constraint from the M53 pulsars. For each constraint, we derive corresponding values of M_{CGM} from an integrated β profile for different values of β . A useful joint constraint on M_{CGM} and β is not possible with the data in hand. The results are shown in Figure 8.

For typical values of β of between 0.4 and 0.5, the DM of FRB 20220319D implies an upper limit on $\log M_{\text{CGM}}$ of between 11.0 and 10.8. The M53 pulsars are even more constraining, limiting $\log M_{\text{CGM}}$ to below a value of between 10.7 to 10.5. We consider the FRB 20220319D constraints to be more conservative because the M53 estimate of DM_{CGM} is very sensitive to the assumed DM_{ISM} along its sightline. The mass constraints all favor values of $f_{\text{CGM}} < 0.5$ (recall $f_{\text{CGM}} = \frac{M_{\text{CGM}} \Omega_b}{M_{\text{tot}}}$) for our fiducial value of $M_{\text{tot}} = 1.5 \times 10^{12} M_\odot$, with M53 potentially accommodating values of $f_{\text{CGM}} \lesssim 0.2$ for reasonable values of β .

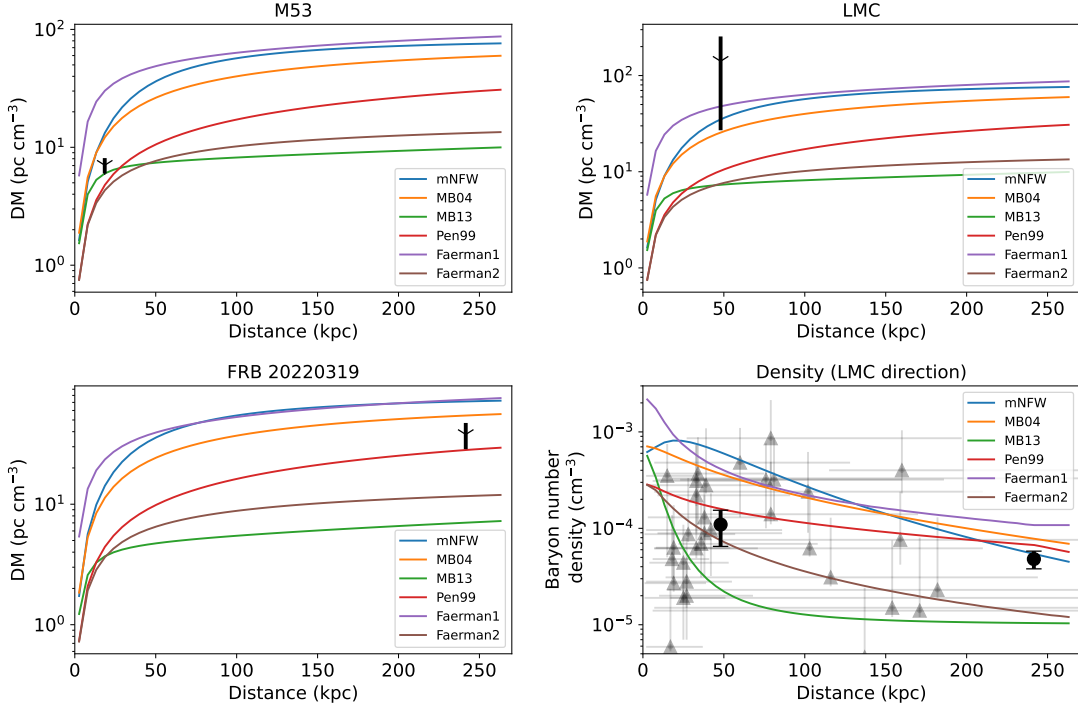


Figure 7. Illustration of the constraining power of different measurements of the CGM DM and density on a range of models. In all panels, curves show predictions of the default modified NFW (mNFW) model of Prochaska & Zheng (2019) (blue), the model of Maller & Bullock (2004) (orange; MB04), the model of Miller & Bregman (2013) (green; MB13), a Pen (1999) model (Pen99) assuming a core radius set to the virial radius (red), and the models of Faerman et al. (2017) (purple; Faerman1) and Faerman et al. (2020) (brown; Faerman2). *Top panels:* upper limit on the CGM DM towards M53 (left) and the LMC (right). In both cases, the minimum DM (18 pc cm^{-3}) across the sky in either the NE2001 or YMW16 models has been subtracted. The ranges indicate the range of DMs of pulsars associated with each object. *Bottom left:* upper limit on the CGM DM towards FRB 20220319D. The range indicates different assumptions for the ISM DM that correspond to the two closest pulsars on the sky. *Bottom right:* constraints on the CGM density compared with the models. The dark disks indicate measurements using ram-pressure stripping modeling of the LMC (Salem et al. 2015) and modeling of diffuse X-ray line emission (Kaaret et al. 2020). The lower limits displayed as triangles indicate estimates using ram-pressure stripping modeling of a large selection of Milky Way satellites (Putman et al. 2021).

6. DISCUSSION

Our results demonstrate that the total Galactic baryon mass is likely significantly lower than the cosmological average for a halo as massive as the Milky Way. The mass constraints we derive are consistent with some previous observational results from analyses of OVII and OVIII emission and absorption (e.g., Li & Bregman 2017; Kaaret et al. 2020) and ram-pressure stripping of the LMC (Salem et al. 2015), but inconsistent with other results that posit higher CGM masses (e.g., Faerman et al. 2017; Yamasaki & Totani 2020). Analyses of the dynamics of Milky Way satellites imply a total virial mass of $M_{\text{tot}} = (1.4 \pm 0.3) \times 10^{12} M_{\odot}$ (Watkins et al. 2010), a recent *Gaia*-based analysis of the dynamics of Milky Way globular clusters yields $M_{\text{tot}} = (1.3 \pm 0.3) \times 10^{12} M_{\odot}$ (Posti & Helmi 2019), and an analysis of the dynamics of the Magellanic Stream yields $M_{\text{tot}} = (1.5 \pm 0.3) \times 10^{12} M_{\odot}$ (Craig et al. 2022). It is possible that a full accounting for the orbit of the

LMC would reduce the estimates of M_{tot} by $\sim 15\%$ (Correa Magnus & Vasiliev 2022). However, in all cases $f_{\text{CGM}} \lesssim 0.4$ is implied by FRB 20220319D, and $f_{\text{CGM}} \lesssim 0.2$ is implied by the M53 DM. Our constraints are affected by different systematic effects to previous results, and do not suffer from uncertainties in modeling the chemical and thermal states of the CGM, nor from uncertainties in modeling the interaction of satellite galaxies with the CGM. These values are consistent with several simulations of the CGM contents of galaxies like the Milky Way that account for the effects of kinetic and thermal feedback on reducing the halo baryon content.

The observational constraints on M_{CGM} are affected by uncertainties in identifying the CGM DM contribution along the sightlines of interest. For the low-latitude FRB 20220319D sightline, we adopted conservative estimates of DM_{ISM} , and there are uncertainties at the level of a few pc cm^{-3} in the DM_{IGM} and DM_{host}

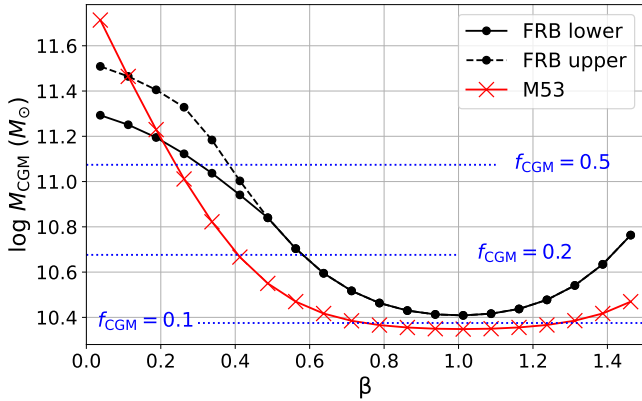


Figure 8. Upper limits on the CGM mass for different assumptions for the radial density profile. We adopt a β model (see text for details), and show limits corresponding to the upper and lower ends of the range of constraints from FRB 20220319D (dashed and solid lines respectively), and from the most constraining pulsar in M53 (red solid line). Typical values of β found in the literature are $\gtrsim 0.4$. For these values, the inferred f_{CGM} values are typically below 0.5, as indicated by blue horizontal lines.

terms. We therefore consider the constraints on M_{CGM} based on FRB 20220319D to be robust to uncertainties in DM_{CGM} . The impact of uncertainty in DM_{ISM} for the M53 sightline is greater given the low values of DM_{CGM} under consideration. Although we attempt to be conservative, even a few-unit increase in DM_{CGM} would significantly raise the derived upper limits on M_{CGM} . Our analysis is also sensitive to how we model the distribution of baryons in the CGM. First, we do not account for sightline to sightline variance, which simulations suggest may be at the level of $\gtrsim 10\%$ (e.g., Zheng et al. 2020; Ramesh et al. 2022). Second, it may be that a β profile is not the correct model to adopt, and our constraints are sensitive to the specific value of β . Guidance on these points from simulations for future analyses of DM_{CGM} will be important. Finally, although we assume a specific helium abundance in translating the DM constraints to a total CGM mass, our results are sensitive to variations in this assumption only at the $< 10\%$ level.

The discovery of FRB 20220319D has major implications for the search for FRBs in the local universe, and for future FRB studies of the CGM of the Milky Way and other galaxies. First, we have shown that for low Galactic latitudes ($|b| \lesssim 15^\circ$; see Figure 4) there can be significant uncertainties in the widely used NE2001 and YMW16 models for DM_{ISM} , which may lead to nearby extragalactic FRBs being missed in surveys. In all cases we recommend that FRB surveys save candidates at DMs below the model values of DM_{ISM} . The possibility of missing FRBs with low extragalactic DMs

also needs to be considered when using FRB samples to directly infer a characteristic DM_{CGM} (e.g., Platts et al. 2020). These studies are also likely to be impacted by the uncertainties in deriving DM_{CGM} that in most cases will be on the order of the values of DM_{CGM} allowed by our analysis (see Figure 7). We recommend that inferences of DM_{CGM} with FRBs focus on high-latitude sightlines towards FRBs interferometrically localized to nearby galaxies, wherein uncertainties in DM_{IGM} and DM_{host} can be minimized. Nonetheless, if the characteristic DM_{CGM} is indeed on the order of 10 pc cm^{-3} , a very large number of local FRBs will be required to suppress variance between halo sightlines, and uncertainties in other DM contributions. These samples may be furnished by future coherent all-sky radio monitors (e.g., Lin et al. 2022). Finally, consistent with previous studies (Keating & Pen 2020; Kirsten et al. 2022), our constraints on f_{CGM} firmly exclude the fiducial parameterizations of the widely used modified-NFW and Maller & Bullock (2004) models for the CGM DM as described by Prochaska & Zheng (2019). This impacts studies that have assumed the correspondingly large values of DM_{CGM} (e.g., Ravi 2019), as well as forecasts for the contributions of the CGM of intervening galaxies to FRB DMs.

The host of FRB 20220319D, IRAS 02044+7048, appears to have an unusually large specific SFR. This is despite FRB 20220319D being the closest so far non-repeating FRB yet discovered, and the strong evolution towards higher SFRs of the star-forming main sequence of galaxies with redshift (Speagle et al. 2014). Our analysis of the SFH of the IRAS 02044+7048 host galaxy suggests that most stars were formed in a burst in the last $\lesssim 2 \text{ Gyr}$. Thus it is likely that the progenitor of FRB 20220319D does not have a delay time (i.e., age from its formation epoch) in excess of this timescale. Although several progenitor scenarios remain consistent with this constraint, the additional possible association of the FRB source with a spiral arm may imply a progenitor age that is a fraction of a $\sim 100 \text{ Myr}$ dynamical timescale. We note that it is not straightforward to compare our inferred SFR, which is averaged over the past 100 Myr of the SFH, to the $\text{H}\alpha$ -based SFRs common in the FRB literature (e.g., Bhandari et al. 2022), which are sensitive to the last $\sim 10 \text{ Myr}$ (Kennicutt 1998). A direct comparison of non-parametric SFH estimates may lead to a more complete view of the formation channels of FRB progenitors.

7. SUMMARY AND CONCLUSIONS

We present the DSA-110 discovery and interferometric localization of the nearest so far non-repeating

FRB (20220319). The burst was observed with a high S/N of 79, a DM of $110.95 \text{ pc cm}^{-3}$, and has a linear polarization fraction of $16 \pm 3\%$ and an RM of $50 \pm 15 \text{ rad m}^{-2}$ (Figure 1, and Table 1). The FRB originated from the position (R.A. J2000, decl. J2000) = (02:08:42.7(1), +71:02:06.9(6)), where uncertainties in the last significant figures are given in parentheses (Figure 2). We associate FRB 20220319D with a spiral-arm feature of a face-on star-forming galaxy at a distance of 50 Mpc (IRAS 02044+7048; Figures 3 and 5; Table 3). IRAS 02044+7048 is moderately massive ($\log M_* = 9.93 \pm 0.07$), with an approximately solar metallicity and an SFR averaged over the past 100 Myr of $1.8 \pm 0.7 M_\odot \text{ yr}^{-1}$ (Figure 6). The low DM of FRB 20220319D motivates a sensitive new constraint on the baryon mass of the Milky Way CGM. Our conclusions are summarized as follows.

- The spatial coincidence of FRB 20220319D and IRAS 02044+7048 (false alarm probability of $< 10^{-4}$), and a potential RM detection for FRB 20220319D that is in excess of the Galactic foreground, both imply a secure association. However, the DM of FRB 20220319D is somewhat lower than the predicted Galactic ISM DM along its sightline from leading models for the WIM distribution (NE2001 and YMW16; Cordes & Lazio 2002; Yao et al. 2017). We show through an analysis of the DMs towards pulsar-hosting globular clusters with *Gaia* parallax distances (Figure 4) that there are significant uncertainties in NE2001 predictions for DM_{ISM} for $|b| \lesssim 15^\circ$, and that YMW16 is particularly uncertain at low latitudes in the second quadrant, where FRB 20220319D is located (see also Table 2). We find that estimates for DM_{ISM} based on H α EMs perform comparably well to the models. We conclude that models for DM_{ISM} towards FRB 20220319D can accommodate an extragalactic origin, and urge FRB surveys to consider candidate bursts at DMs below standard model predictions for DM_{ISM} .
- The SFH of IRAS 02044+7048 is consistent with most stars being formed in a burst within the past two Gigayears. This, together with the possible location of FRB 20220319D within a spiral arm of IRAS 02044+7048, suggests a moderately low delay time for the burst progenitor. Despite its nearby distance, the specific SFR of IRAS 02044+7048 derived from SED modeling is larger than all but one so far non-repeating FRB, although the comparison with literature samples

of host galaxies would be aided by the widespread use of non-parametric SFH analyses.

- We find conservative upper limits on the Galactic CGM contribution to the DM of FRB 20220319D of either 28.7 pc cm^{-3} or 47.3 pc cm^{-3} : the two values are based on DM_{ISM} -estimates from the DMs of two pulsars nearby on the sky. These limits exclude some literature models (Maller & Bullock 2004; Faerman et al. 2017; Prochaska & Zheng 2019) for the baryon distribution in the CGM (Figure 7). We find that consistent results are obtained from estimates of the CGM DM contributions towards pulsars in the LMC and in the distant (18.5 kpc) high-latitude globular cluster M53. The M53 pulsars in particular provide interesting constraints in the inner regions of the Milky Way halo that complement the FRB constraint, although the M53 DM_{CGM} estimate is sensitive to the assumed ISM contribution.
- We derive an upper limit on the mass of baryons in the Galactic CGM of $\log M_{\text{CGM}} \lesssim 10.8 - 11$ from FRB 20220319D, and $\log M_{\text{CGM}} \lesssim 10.5 - 10.7$ from M53 (Figure 8). The range corresponds to the range of assumed indices (0.4–0.5) of the β profile for the baryon halo density distribution. For a fiducial total mass (baryons and dark matter) of the Milky Way of $1.5 \times 10^{12} M_\odot$, and an assumed baryon-disk mass of $6 \times 10^{10} M_\odot$, the Milky Way contains $\ll 60\%$ of the cosmological-average baryon mass. This is consistent with a baryon census, predicted by galaxy-formation simulations, wherein these “missing” baryons are expelled from halos like the Milky Way into the IGM through kinetic and thermal feedback from AGN, supernovae and massive stars. Although our analysis relies on just a few sightlines, the conservative upper bounds on M_{CGM} assuming spherical symmetry are robust to variations in the density distribution of halo baryons, and to assumptions on the chemical and thermal state of the halo.

Studies of unseen baryons with FRB propagation signatures, like DMs, promise to transform our understanding of the distribution of baryons around and in between galaxies (Ravi et al. 2019). As more FRBs like FRB 20220319D are localized to nearby galaxies (see also Kirsten et al. 2022), constraints on the CGM content of the Milky Way will continue to improve, and direct measurements of M_{CGM} may be possible. These measurements are likely to be important in assembling an in-situ picture of the processes whereby a galaxy grows from and impacts its environment.

The authors thank staff members of the Owens Valley Radio Observatory and the Caltech radio group, including Kristen Bernasconi, Stephanie Cha-Ramos, Sarah Harnach, Tom Klinefelter, Lori McGraw, Corey Posner, Andres Rizo, Michael Virgin, Scott White, and Thomas Zentmyer. Their tireless efforts were instrumental to the success of the DSA-110. The DSA-110 is supported by the National Science Foundation Mid-Scale Innovations Program in Astronomical Sciences (MSIP) under grant AST-1836018. We acknowledge use of the VLA calibrator manual and the radio fundamental catalog. Some of the data presented herein were obtained at the W. M. Keck Observatory, which is operated as a scientific partnership among the California Institute of Technology, the University of California and the National Aeronautics and Space Administration. The Observatory was made possible by the generous financial support of the W. M. Keck Foundation.

Facility: Hale

Software: astropy, CASA, heimdall, pypeit, Prospector, wsclean

REFERENCES

- Anderson, M. E. & Bregman, J. N. 2010, *ApJ*, 714, 320.
doi:10.1088/0004-637X/714/1/320
- Appleby, S., Davé, R., Sorini, D., et al. 2021, *MNRAS*, 507, 2383. doi:10.1093/mnras/stab2310
- Baldwin, J. E. 1956, Ph.D. Thesis
- Baumgardt, H. & Vasiliev, E. 2021, *MNRAS*, 505, 5957.
doi:10.1093/mnras/stab1474
- Berkhuijsen, E. M., Mitra, D., & Mueller, P. 2006, *Astronomische Nachrichten*, 327, 82.
doi:10.1002/asna.200510488
- Bhandari, S., Sadler, E. M., Prochaska, J. X., et al. 2020, *ApJL*, 895, L37. doi:10.3847/2041-8213/ab672e
- Bhandari, S., Heintz, K. E., Aggarwal, K., et al. 2022, *AJ*, 163, 69. doi:10.3847/1538-3881/ac3aec
- Bhardwaj, M., Kirichenko, A. Y., Michilli, D., et al. 2021, *ApJL*, 919, L24. doi:10.3847/2041-8213/ac223b
- Birnboim, Y. & Dekel, A. 2003, *MNRAS*, 345, 349.
doi:10.1046/j.1365-8711.2003.06955.x
- Bochenek, C. D., Ravi, V., & Dong, D. 2021, *ApJL*, 907, L31. doi:10.3847/2041-8213/abd634
- Bregman, J. N. & Lloyd-Davies, E. J. 2007, *ApJ*, 669, 990.
doi:10.1086/521321
- Bregman, J. N., Hodges-Kluck, E., Qu, Z., et al. 2022, *ApJ*, 928, 14. doi:10.3847/1538-4357/ac51de
- Carretti, E., Crocker, R. M., Staveley-Smith, L., et al. 2013, *Nature*, 493, 66. doi:10.1038/nature11734
- Clark, S., Bordoloi, R., & Fox, A. J. 2022, *MNRAS*, 512, 811. doi:10.1093/mnras/stac504
- Chambers, K. C., Magnier, E. A., Metcalfe, N., et al. 2016, arXiv:1612.05560
- Condon, J. J., Cotton, W. D., Greisen, E. W., et al. 1998, *AJ*, 115, 1693. doi:10.1086/300337
- Connor, L., van Leeuwen, J., Oostrum, L. C., et al. 2020, *MNRAS*, 499, 4716. doi:10.1093/mnras/staa3009
- Connor, L. & Ravi, V. 2022, *Nature Astronomy*, 6, 1035.
doi:10.1038/s41550-022-01719-7
- Cordes, J. M. & Lazio, T. J. W. 2002, astro-ph/0207156
- Cordes, J. M., Ocker, S. K., & Chatterjee, S. 2022, *ApJ*, 931, 88. doi:10.3847/1538-4357/ac6873
- Correa Magnus, L. & Vasiliev, E. 2022, *MNRAS*, 511, 2610.
doi:10.1093/mnras/stab3726
- Craig, P. A., Chakrabarti, S., Baum, S., et al. 2022, *MNRAS*, 517, 1737. doi:10.1093/mnras/stac2308
- Cutri, R. M., Wright, E. L., Conrow, T., et al. 2021, *VizieR Online Data Catalog*, II/328
- Deller, A. T., Goss, W. M., Brisken, W. F., et al. 2019, *ApJ*, 875, 100. doi:10.3847/1538-4357/ab11c7
- Draine, B. T. 2011, *Physics of the Interstellar and Intergalactic Medium* by Bruce T. Draine. Princeton University Press, 2011. ISBN: 978-0-691-12214-4
- Faerman, Y., Sternberg, A., & McKee, C. F. 2017, *ApJ*, 835, 52. doi:10.3847/1538-4357/835/1/52
- Faerman, Y., Sternberg, A., & McKee, C. F. 2020, *ApJ*, 893, 82. doi:10.3847/1538-4357/ab7ffc
- Fielding, D. B., Tonnesen, S., DeFelippis, D., et al. 2020, *ApJ*, 903, 32. doi:10.3847/1538-4357/abbc6d

- Fitzpatrick, E. L. & Massa, D. 2007, *ApJ*, 663, 320.
doi:10.1086/518158
- Foreman-Mackey, D., Hogg, D. W., Lang, D., et al. 2013, *PASP*, 125, 306. doi:10.1086/670067
- Garmire, G. P., Nousek, J. A., Apparao, K. M. V., et al. 1992, *ApJ*, 399, 694. doi:10.1086/171962
- GRAVITY Collaboration, Abuter, R., Amorim, A., et al. 2019, *A&A*, 625, L10. doi:10.1051/0004-6361/201935656
- Gupta, A., Mathur, S., Krongold, Y., et al. 2012, *ApJL*, 756, L8. doi:10.1088/2041-8205/756/1/L8
- HI4PI Collaboration, Ben Bekhti, N., Flöer, L., et al. 2016, *A&A*, 594, A116. doi:10.1051/0004-6361/201629178
- Hafen, Z., Faucher-Giguère, C.-A., Anglés-Alcázar, D., et al. 2020, *MNRAS*, 494, 3581. doi:10.1093/mnras/staa902
- Haffner, L. M., Reynolds, R. J., Tufte, S. L., et al. 2003, *ApJS*, 149, 405. doi:10.1086/378850
- He, C., Ng, C.-Y., & Kaspi, V. M. 2013, *ApJ*, 768, 64. doi:10.1088/0004-637X/768/1/64
- Heintz, K. E., Prochaska, J. X., Simha, S., et al. 2020, *ApJ*, 903, 152. doi:10.3847/1538-4357/abb6fb
- Herbstmeier, U., Mebold, U., Snowden, S. L., et al. 1995, *A&A*, 298, 606
- Ho, L. C., Filippenko, A. V., & Sargent, W. L. W. 1997, *ApJS*, 112, 315. doi:10.1086/313041
- Hutschenreuter, S., Anderson, C. S., Betti, S., et al. 2022, *A&A*, 657, A43. doi:10.1051/0004-6361/202140486
- Johnson, B. D., Leja, J., Conroy, C., et al. 2021, *ApJS*, 254, 22. doi:10.3847/1538-4365/abef67
- Kaaret, P., Koutroumpa, D., Kuntz, K. D., et al. 2020, *Nature Astronomy*, 4, 1072. doi:10.1038/s41550-020-01215-w
- Keating, L. C. & Pen, U.-L. 2020, *MNRAS*, 496, L106. doi:10.1093/mnras/slaa095
- Kennicutt, R. C. 1998, *ARA&A*, 36, 189. doi:10.1146/annurev.astro.36.1.189
- Kewley, L. J., Groves, B., Kauffmann, G., et al. 2006, *MNRAS*, 372, 961. doi:10.1111/j.1365-2966.2006.10859.x
- Kirsten, F., Marcote, B., Nimmo, K., et al. 2022, *Nature*, 602, 585. doi:10.1038/s41586-021-04354-w
- Koo, B.-C., Heiles, C., & Reach, W. T. 1992, *ApJ*, 390, 108. doi:10.1086/171264
- Kulkarni, S. R., Anderson, S. B., Prince, T. A., et al. 1991, *Nature*, 349, 47. doi:10.1038/349047a0
- Leja, J., Carnall, A. C., Johnson, B. D., et al. 2019, *ApJ*, 876, 3. doi:10.3847/1538-4357/ab133c
- Li, Y. & Bregman, J. 2017, *ApJ*, 849, 105. doi:10.3847/1538-4357/aa92c6
- Li, J.-T., Bregman, J. N., Wang, Q. D., et al. 2018, *ApJL*, 855, L24. doi:10.3847/2041-8213/aab2af
- Lin, H.-H., Lin, K.-yang, Li, C.-T., et al. 2022, *PASP*, 134, 094106. doi:10.1088/1538-3873/ac8f71
- Macquart, J.-P., Prochaska, J. X., McQuinn, M., et al. 2020, *Nature*, 581, 391. doi:10.1038/s41586-020-2300-2
- Madsen, G. J. & Reynolds, R. J. 2005, *ApJ*, 630, 925. doi:10.1086/432043
- Maller, A. H. & Bullock, J. S. 2004, *MNRAS*, 355, 694. doi:10.1111/j.1365-2966.2004.08349.x
- Manchester, R. N., Hobbs, G. B., Teoh, A., et al. 2005, *AJ*, 129, 1993. doi:10.1086/428488
- Mannings, A. G., Fong, W.-fai, Simha, S., et al. 2021, *ApJ*, 917, 75. doi:10.3847/1538-4357/abff56
- Miller, M. J. & Bregman, J. N. 2013, *ApJ*, 770, 118. doi:10.1088/0004-637X/770/2/118
- Miller, M. J. & Bregman, J. N. 2015, *ApJ*, 800, 14. doi:10.1088/0004-637X/800/1/14
- Moser, E., Battaglia, N., Nagai, D., et al. 2022, *ApJ*, 933, 133. doi:10.3847/1538-4357/ac70c6
- Nakashima, S., Inoue, Y., Yamasaki, N., et al. 2018, *ApJ*, 862, 34. doi:10.3847/1538-4357/aacceb
- Navarro, J. F., Frenk, C. S., & White, S. D. M. 1997, *ApJ*, 490, 493. doi:10.1086/304888
- Normandeau, M., Taylor, A. R., & Dewdney, P. E. 1996, *Nature*, 380, 687. doi:10.1038/380687a0
- Ocker, S. K., Cordes, J. M., & Chatterjee, S. 2020, *ApJ*, 897, 124. doi:10.3847/1538-4357/ab98f9
- Ocker, S. K., Cordes, J. M., Chatterjee, S., et al. 2022, *ApJ*, 934, 71. doi:10.3847/1538-4357/ac75ba
- Oke, J. B. & Gunn, J. E. 1982, *PASP*, 94, 586. doi:10.1086/131027
- Pan, Z., Qian, L., Ma, X., et al. 2021, *ApJL*, 915, L28. doi:10.3847/2041-8213/ac0bbd
- Pen, U.-L. 1999, *ApJL*, 510, L1. doi:10.1086/311799
- Planck Collaboration, Aghanim, N., Akrami, Y., et al. 2020, *A&A*, 641, A6. doi:10.1051/0004-6361/201833910
- Platts, E., Prochaska, J. X., & Law, C. J. 2020, *ApJL*, 895, L49. doi:10.3847/2041-8213/ab930a
- Pleunis, Z., Good, D. C., Kaspi, V. M., et al. 2021, *ApJ*, 923, 1. doi:10.3847/1538-4357/ac33ac
- Posti, L. & Helmi, A. 2019, *A&A*, 621, A56. doi:10.1051/0004-6361/201833355
- Predehl, P., Sunyaev, R. A., Becker, W., et al. 2020, *Nature*, 588, 227. doi:10.1038/s41586-020-2979-0
- Price, D. C., Flynn, C., & Deller, A. 2021, *PASA*, 38, e038. doi:10.1017/pasa.2021.33
- Prochaska, J. X. & Zheng, Y. 2019, *MNRAS*, 485, 648. doi:10.1093/mnras/stz261
- Prochaska, J., Hennawi, J., Westfall, K., et al. 2020, *The Journal of Open Source Software*, 5, 2308. doi:10.21105/joss.02308

- Putman, M. E., Peek, J. E. G., & Jounge, M. R. 2012, *ARA&A*, 50, 491.
doi:10.1146/annurev-astro-081811-125612
- Putman, M. E., Zheng, Y., Price-Whelan, A. M., et al. 2021, *ApJ*, 913, 53. doi:10.3847/1538-4357/abe391
- Ramesh, R., Nelson, D., & Pillepich, A. 2022, arXiv:2211.00020
- Ravi, V. 2019, *Nature Astronomy*, 3, 928.
doi:10.1038/s41550-019-0831-y
- Ravi, V., Battaglia, N., Burke-Spolaor, S., et al. 2019, *BAAS*, 51, 420
- Ravi, V., Catha, M., Chen, G., et al. 2022, arXiv:2211.09049
- Rees, M. J. & Ostriker, J. P. 1977, *MNRAS*, 179, 541.
doi:10.1093/mnras/179.4.541
- Reid, M. J., Schneps, M. H., Moran, J. M., et al. 1988, *ApJ*, 330, 809. doi:10.1086/166514
- Ridley, J. P., Crawford, F., Lorimer, D. R., et al. 2013, *MNRAS*, 433, 138. doi:10.1093/mnras/stt709
- Salem, M., Besla, G., Bryan, G., et al. 2015, *ApJ*, 815, 77.
doi:10.1088/0004-637X/815/1/77
- Schlaflly, E. F. & Finkbeiner, D. P. 2011, *ApJ*, 737, 103.
doi:10.1088/0004-637X/737/2/103
- Schnitzeler, D. H. F. M. 2012, *MNRAS*, 427, 664.
doi:10.1111/j.1365-2966.2012.21869.x
- Seebeck, J., Ravi, V., Connor, L., et al. 2021, arXiv:2112.07639
- Skrutskie, M. F., Cutri, R. M., Stiening, R., et al. 2006, *AJ*, 131, 1163. doi:10.1086/498708
- Snowden, S. L., Mebold, U., Hirth, W., et al. 1991, *Science*, 252, 1529. doi:10.1126/science.252.5012.1529
- Speagle, J. S., Steinhardt, C. L., Capak, P. L., et al. 2014, *ApJS*, 214, 15. doi:10.1088/0067-0049/214/2/15
- Spitzer, L. 1956, *ApJ*, 124, 20. doi:10.1086/146200
- Su, M., Slatyer, T. R., & Finkbeiner, D. P. 2010, *ApJ*, 724, 1044. doi:10.1088/0004-637X/724/2/1044
- Tendulkar, S. P., Gil de Paz, A., Kirichenko, A. Y., et al. 2021, *ApJL*, 908, L12. doi:10.3847/2041-8213/abdb38
- Tumlinson, J., Thom, C., Werk, J. K., et al. 2011, *Science*, 334, 948. doi:10.1126/science.1209840
- Tumlinson, J., Peebles, M. S., & Werk, J. K. 2017, *ARA&A*, 55, 389.
doi:10.1146/annurev-astro-091916-055240
- Ueda, M., Sugiyama, H., Kobayashi, S. B., et al. 2022, *PASJ*, 74, 1396. doi:10.1093/pasj/psac077
- Vasiliev, E. & Baumgardt, H. 2021, *MNRAS*, 505, 5978.
doi:10.1093/mnras/stab1475
- Watkins, L. L., Evans, N. W., & An, J. H. 2010, *MNRAS*, 406, 264. doi:10.1111/j.1365-2966.2010.16708.x
- Werk, J. K., Rubin, K. H. R., Bish, H. V., et al. 2019, *ApJ*, 887, 89. doi:10.3847/1538-4357/ab54cf
- White, S. D. M. & Rees, M. J. 1978, *MNRAS*, 183, 341.
doi:10.1093/mnras/183.3.341
- White, D. J., Daw, E. J., & Dhillon, V. S. 2011, *Classical and Quantum Gravity*, 28, 085016.
doi:10.1088/0264-9381/28/8/085016
- Wijers, N. A., Schaye, J., & Oppenheimer, B. D. 2020, *MNRAS*, 498, 574. doi:10.1093/mnras/staa2456
- Wu, X. & McQuinn, M. 2022, arXiv:2209.04455
- Yamasaki, S. & Totani, T. 2020, *ApJ*, 888, 105.
doi:10.3847/1538-4357/ab58c4
- Yao, J. M., Manchester, R. N., & Wang, N. 2017, *ApJ*, 835, 29. doi:10.3847/1538-4357/835/1/29
- Zheng, Y., Peebles, M. S., O'Shea, B. W., et al. 2020, *ApJ*, 896, 143. doi:10.3847/1538-4357/ab960a